Key Points:
- New analytical solutions are presented for steady, barotropic, wind- and boundary-driven planetary geostrophic circulation in a circular polar basin with a step shelf
- The partition of water entering the Arctic into clockwise and anticlockwise shelf currents is sensitive to shelf width variation with longitude
- The steady circulation is topographically steered, and therefore, a transpolar drift current is supported by a transpolar ridge

Correspondence to:
E. Gavilan Pascual-Ahuir,
e.gavilan@hhu.edu.cn

Topographical Control of the Source-Sink and Wind Stress-Driven Planetary Geostrophic Circulation in a Polar Basin

Estanislao Gavilan Pascual-Ahuir[1,2] (iD), **Andrew J. Willmott[3]**, **Miguel Morales Maqueda[4]**, and **Maria Luneva[5]** (iD)

[1]College of Oceanography, Hohai University, Nanjing, China, [2]Southern Marine Science and Engineering Guangdong Laboratory (Zhuhai), Zhuhai, China, [3]School of Mathematics, Statistics and Physics, Newcastle University, Newcastle upon Tyne, UK, [4]School of Natural and Environmental Sciences, Newcastle University, Newcastle upon Tyne, UK, [5]National Oceanography Centre, Liverpool, UK

Abstract The effects of topography on the barotropic circulation in a polar basin are examined analytically and numerically. New approximate linear analytical solutions are presented for steady-state wind and boundary forced barotropic planetary geostrophic circulation in a circular polar basin with a step shelf. The solutions are obtained by retaining the full spherical geometry in the derivation of the forced potential vorticity equation; thereafter the colatitude is fixed in the coefficients of this governing equation. The accuracy of the analytical solutions is evaluated by comparing them with the equivalent numerical solutions obtained using the NEMO modeling system. Subsequently, the impact of a nonuniform width shelf on source-sink-driven circulation is investigated numerically. The equipartition of fluid entering the source strait into cyclonic and anticyclonic shelf currents, exiting the basin at the sink strait, in a basin with a uniform width shelf is shown to be modified when the shelf width varies. In general, the wider shelf supports a current with larger transport, irrespective of the azimuthal extent of the wider shelf. The study concludes with a numerical investigation of wind-driven circulation in a basin with a step shelf, three straits, and a transpolar ridge, a prototype Arctic Ocean simulation. Topographic steering by the ridge supports a transpolar drift current, the magnitude of which depends on the ridge height. Without the ridge, the transpolar drift current is absent and the circulation is confined to gyres on the shelf and in the deep basin.

Plain Language Summary The direction of the currents in the Arctic Ocean is strongly influenced by the varying depth of the basin. Specifically, the currents attempt to follow paths where the depth does not change. We refer to such currents as being "steered" by the underlying sea bed features, such as the ridges, seamounts and continental shelves. In this study, we describe new mathematical models for predicting the pathways of the Arctic Ocean currents and therefore the importance of the "steering" effect. We demonstrate that the flow of water from the eastern Arctic Siberian shelf across the pole to the western Arctic North American shelf is "steered" by an underwater ridge. Our research suggests that the path of this transpolar current will not change as Arctic summer sea ice disappears in response to global warming.

1. Introduction

Analytical solutions for wind- and boundary-forced barotropic ocean circulation in a polar cap are few and far between in the refereed literature. One reason for this is that on the polar plane, the high-latitude equivalent of the midlatitude β plane, the Coriolis parameter, varies quadratically with meridional distance from the pole (see LeBlond, 1964). In the context of linearized barotropic ocean dynamics on the polar plane, the vorticity equation will therefore have nonconstant coefficients. Nevertheless, Luneva et al. (2012) and Willmott and Luneva (2015) have developed analytical solutions for geostrophic adjustment and steady wind-driven ocean circulation, respectively, in a polar cap using the polar plane approximation. The polar plane approximation is also used by LeBlond (1964) to obtain an analytical dispersion relation for freely propagating divergent planetary waves in a flat bottom ocean in a polar cap.
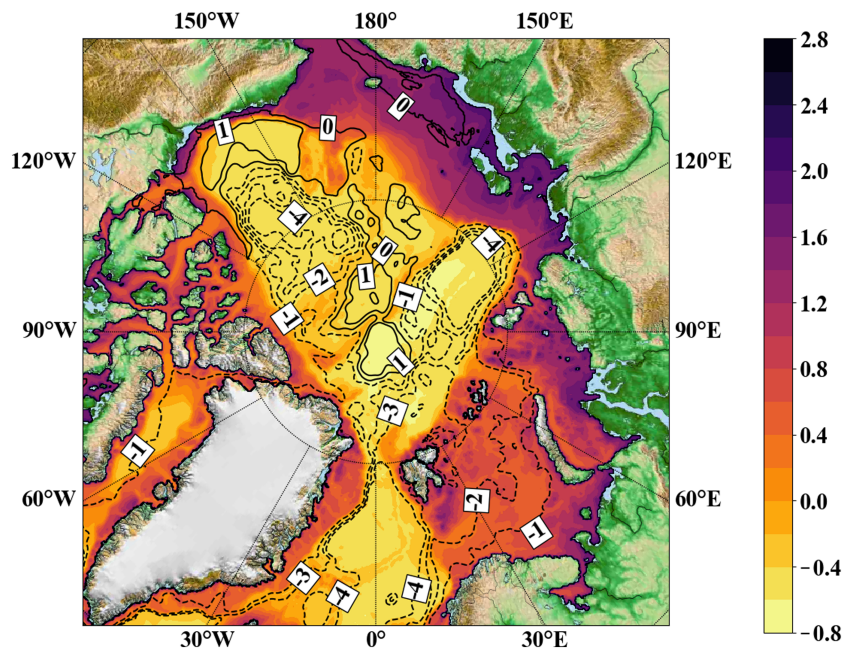
Figure 1. Contours of the mean barotropic streamfunction (in Sv) in the Arctic Ocean for the period January 2003 to December 2011. Shown in color is $\log_{10}(f/(dH))$, where f is the Coriolis parameter, H is ocean depth and $d = 1.405 \times 10^{-5}$ m^{-1} s^{-1} is a normalization constant. The streamfunction was calculated from monthly mean output of the TOPAZ4 model (Sakov et al., 2012).

An alternative approach for developing analytical solutions for barotropic planetary geostrophic ocean circulation in a polar cap was proposed by Imawaki and Takano (1974). In this study the exact vorticity equation is derived in terms of spherical polar coordinates. Thereafter, the colatitudinal dependence of the coefficients in this equation is suppressed by fixing the colatitude at a value midway between the pole and location of the basin boundary. The resulting constant coefficient vorticity equation was then solved analytically using a Fourier method for steady source-sink-driven circulation in a flat bottom polar cap. The ideas discussed in Imawaki and Takano (1974) appear to have been neglected for over 40 years until Willmott and Gavilan Pascual-Ahuir (2017) employ them to derive an approximate dispersion relation for divergent planetary waves in a polar cap, a problem first addressed by LeBlond (1964). A third approach for developing accurate approximations for planetary and gravity wave frequencies in a spherical polar cap is discussed in Bassom and Willmott (2019). In this study the amplitude equation for these waves is analyzed by exploiting a small parameter based on the limited latitudinal extent of the polar basin.

The purpose of this paper is to examine the topographical steering and the role of bottom friction on the structure of barotropic planetary geostrophic circulation in the polar basin. For this purpose we derive new analytical solutions for steady wind and boundary-driven barotropic ocean circulation in a polar basin with a step shelf using the approximate method of Imawaki and Takano (1974). In this latter study topography and wind forcing were not considered. The analytical solutions are also complemented with numerical solutions calculated using the NEMO (Nucleus for European Modelling of the Ocean) general ocean circulation model (Madec, 2008) that include more realistic topography and wind forcing. We then address the relevance of these "reduced physics" barotropic models to the Arctic Ocean circulation.

A natural question to ask is how relevant are barotropic planetary geostrophic dynamics to understanding the observed Arctic Ocean circulation? After all, sea ice and stratification are both neglected in this study. Figure 1 shows a high degree of correlation between the contours of the barotropic streamfunction calculated from the monthly mean output of the TOPAZ ocean circulation model (Sakov et al., 2012) and the isobaths. Contours of the sea surface elevation field (not shown for brevity) averaged over the period 2003 to 2011 exhibit the signature of the Beaufort Gyre consistent with the barotropic streamfunction of Figure 1. This stratified North Atlantic and Arctic Ocean numerical simulation includes sea ice. Although the upper water column is stratified in the Arctic Ocean, the stratification is almost nonexistent below the halocline (Zhao & Timmermans, 2018), which results in significant topographic steering of the barotropic transport.

Table 1
Ocean Basin Parameters Used in the Numerical and Analytical Experiments, Unless Otherwise Stated

Symbol	Variable (Unit)	Value
—	Horizontal resolution (deg)	$1/10 \times 1/10$
—	Vertical resolution (m)	500
—	Time step (s)	1200
A_H	Horizontal Laplacian eddy viscosity (m^2 s^{-1})	500
μ	Bottom drag coefficient (ms^{-1})	1×10^{-4}
H	Depth of flat bottom basin (m)	1,000
H_1	Depth of step shelf (m)	250
H_2	Depth of deep basin (m)	1,000
θ_f	Fixed colatitude in (7) (deg)	10
θ_S	Colatitude on the shelf edge (deg)	10
θ_B	Colatitude of the boundary of the basin (deg)	20
2ϵ	Degrees of longitude spanned by the gaps (deg)	20
T_0	Strength of the prescribed source/sink (Sv; sverdrups)	5

The plan of the paper is as follows. Section 2 summarizes the NEMO model implementation; Section 3 presents analytical solutions for steady source-sink-driven flows in a polar basin with a step shelf using the method of Imawaki and Takano (1974), and these are compared with the equivalent numerical solutions using the NEMO GCM; section 4 extends the solutions in the previous section to include idealized wind stress driving; section 5 presents numerical simulations of wind-driven steady-state circulation in a basin with a step shelf and three straits. These latter numerical simulations are a step closer to simulating the observed Arctic Ocean circulation. In particular, the wind stress fields used in section 5 are representative of the observed anticyclonic and cyclonic Arctic wind stress fields. Of course, direct comparison of the results in this paper with observations in the Arctic Ocean must be carried out cautiously because stratification and sea ice are omitted. These points are discussed in section 6.

2. NEMO Model Description

All the numerical simulations discussed in this paper employ the nonlinear three-dimensional ocean circulation model NEMO (Madec, 2008). Following Luneva et al. (2012) we use a filtered nonlinear free surface algorithm, which is stable with relatively large time steps but damps the fast gravity and inertia-gravity waves. Planetary waves, are however, resolved using this algorithm.

The geographical domain is a circular basin where the North Pole is located in the center of the grid. However, the computational domain is defined by the rotation of geographical coordinates. This transformation places the North Pole into the equatorial plane avoiding the coordinate singularity. Table 1 lists the parameter values used in the control experiment, namely a flat bottom basin with two diametrically opposed gaps. Across one gap a uniform inflow is prescribed (i.e., a source) and across the opposite gap, an equal but opposite outflow (i.e., a sink) is prescribed. Unless otherwise stated, the same parameters are used in all NEMO experiments.

3. Source-Sink-Driven Planetary Geostrophic Circulation in a Polar Basin With a Step Shelf

3.1. Governing Equations

We consider an ocean of uniform density, ρ, on a polar cap. A spherical polar coordinate system is adopted where θ and φ denote the colatitude and longitude (i.e., azimuthal) angle, respectively, and θ_B is the colatitude of the boundary of the polar cap. Therefore, $\theta \in [0, \theta_B)$ and $\varphi \in [0, 2\pi)$. The unit vectors $\mathbf{k}$, $\hat{\theta}$, and $\hat{\varphi}$ in the respective directions of r, θ, and φ increasing form a right-handed triad where

$$\mathbf{k} \wedge \hat{\theta} = \hat{\varphi}.$$

The steady-state linearized shallow water momentum equations take the form

$$f\mathbf{k} \times \mathbf{u} = -g\nabla\eta + \text{Dissipation} + \frac{\boldsymbol{\tau}}{\rho H}, \tag{1}$$

where $\mathbf{u} = u\hat{\varphi} + v\hat{\theta}$, $f = 2\Omega\cos\theta$, τ is the wind stress, η is the dynamic free surface elevation, and g is the gravitational acceleration. We consider two forms of the dissipation term:

$$-\frac{\mu}{H}\mathbf{u}, \tag{2a}$$

$$\frac{A_H}{R^2}\mathbf{u}_{\theta\theta}. \tag{2b}$$

Expression (2a) represents linear (Rayleigh) bottom friction, where μ is the constant bottom friction parameter and H is the undisturbed ocean depth. Alternatively, we introduce an approximate form for the eddy diffusivity in equation (2b), where A_H is the constant eddy diffusivity and R is the radius of the Earth. Imawaki and Takano (1974) adopt the Laplacian eddy diffusivity $A_H\nabla_H^2\mathbf{u}$ in their study of source-sink-driven flow on a flat bottom spherical cap, where ∇_H^2 is the Laplacian operator. We extend the solutions of Imawaki and Takano by introducing a step shelf, but in doing so, we retain the dominant terms in the Laplacian frictional boundary layers that are present at the uniform width shelf edge, $\theta = \theta_S$, and adjacent to the polar cap boundary $\theta = \theta_B$. Therefore, equation (2b) retains the term with the highest number of derivatives in the $\hat{\theta}$ direction which is a familiar approach in the analysis of boundary layer dynamics. We bear in mind that this approach is less suitable near the straits, but we apply it everywhere for mathematical convenience. A rigid-lid approximation is adopted allowing the introduction of a transport streamfunction $\psi(\varphi, \theta)$ where

$$Hu = \frac{1}{R}\psi_\theta, \qquad Hv = \frac{-1}{R\sin\theta}\psi_\varphi. \tag{3}$$

3.2. Circulation in a Step-Shelf Basin With Bottom Friction
In this subsection solutions for the steady-state circulation driven by prescribed inflow/outflow across two open boundaries are derived in a basin with a step shelf. The basin topography is given by

$$H(\theta) = \begin{cases} H_1, \ \theta_S \leq \theta \leq \theta_B, \\ H_2, \ 0 \leq \theta \leq \theta_S, \end{cases} \tag{4}$$

where $H_1 < H_2$. Let $\psi_1(\varphi, \theta)$ and $\psi_2(\varphi, \theta)$ denote the streamfunction on the shelf $\theta_S \leq \theta \leq \theta_B$ and in the deep basin $0 \leq \theta \leq \theta_S$, respectively. Taking the curl of equation (1) we obtain the vorticity equations on the shelf and in the deep basin:

$$\psi_{1\varphi\varphi} + A\psi_{1\theta\theta} + B\psi_{1\theta} + C_1\psi_{1\varphi} = 0, \tag{5a}$$

$$\psi_{2\varphi\varphi} + A\psi_{2\theta\theta} + B\psi_{2\theta} + C_2\psi_{2\varphi} = 0, \tag{5b}$$

upon setting $\tau = 0$ and adopting bottom friction (2a). The coefficients A, B, and $C_j(j = 1, 2)$ in equation (5) are defined as

$$A \equiv \sin^2\theta, \quad B \equiv \sin\theta\cos\theta, \quad C_1 \equiv \gamma\sin^2\theta, \quad C_2 \equiv \gamma\left(\frac{H_2}{H_1}\right)\sin^2\theta, \tag{6}$$

where $\gamma = 2\Omega H_1\mu^{-1}$.

We note that the relative effects of rotation, friction, and ocean depth are combined in a single dimensionless parameter γ. As the ocean depth increases, or bottom friction decreases, we see that γ increases and rotation has a greater influence on the circulation. Following Imawaki and Takano (1974), we fix $\theta = \theta_f$ in equation (6), the typical value being midway between the pole and $\theta = \theta_B$. Then equation (5) becomes constant coefficient linear second-order partial differential equations, which can be solved using classical analytical techniques.

On the boundary of the basin we prescribe an inward volume transport of magnitude T_0 through the strait $[-\epsilon \leq \varphi \leq \epsilon]$ balanced by an equal outflow through the strait $[\pi - \epsilon \leq \varphi \leq \pi + \epsilon]$. Mathematically, this is achieved by the following boundary condition

$$\psi_1\left(\varphi, \theta_B\right) \equiv \psi_{1B} = \psi_0 \begin{cases} \varphi/\epsilon & if & 0 \leq \varphi \leq \epsilon, \\ 1 & if & \epsilon \leq \varphi \leq \pi - \epsilon, \\ 1 - \left[\varphi - (\pi - \epsilon)\right]/\epsilon & if & \pi - \epsilon \leq \varphi \leq \pi + \epsilon, \\ -1 & if & \pi + \epsilon \leq \varphi \leq 2\pi - \epsilon, \\ -1 + \left[\varphi - (2\pi - \epsilon)\right]/\epsilon & if & 2\pi - \epsilon \leq \varphi \leq 2\pi. \end{cases} \tag{7}$$

At the pole equation (5b) requires that

$$\psi_{2\varphi\varphi} = 0 \quad at \quad \theta = 0, \tag{8}$$

while at the shelf edge we demand continuity of the meridional transport and pressure. Continuity of meridional transport is satisfied provided

$$\psi_1 = \psi_2 \quad at \quad \theta = \theta_S. \tag{9}$$

Using equations (1) and (2a), the latter matching condition requires that

$$\left[fv + \mu \frac{u}{H}\right] = 0, \quad at \quad \theta = \theta_S, \tag{10}$$

where the square brackets in equation (10) denote the "jump condition" across the shelf edge. In terms of the transport streamfunction equation (10) becomes

$$\left[\frac{-f\psi_\varphi}{HR \sin\theta} + \frac{\mu\psi_\theta}{H^2 R}\right] = 0, \quad at \quad \theta = \theta_S. \tag{11}$$

We seek solutions of equation (5) of the form

$$\psi_1(\varphi, \theta) = a_0(\theta) + \sum_{n=1}^{\infty} \left[a_n(\theta) \cos n\varphi + b_n(\theta) \sin n\varphi\right], \tag{12a}$$

$$\psi_2(\varphi, \theta) = A_0(\theta) + \sum_{n=1}^{\infty} \left[A_n(\theta) \cos n\varphi + B_n(\theta) \sin n\varphi\right]. \tag{12b}$$

It is convenient to introduce the following complex functions

$$z_n = a_n + ib_n, \quad Z_n = A_n + iB_n, \quad n \geq 1, \tag{13}$$

to solve the above boundary value problem. In terms of these functions the shelf-edge matching conditions (9) and (11) become

$$z_n = Z_n \quad at \quad \theta = \theta_S, \tag{14a}$$

and

$$\frac{H_1 f_S}{\sin\theta_S} i n z_n + \mu \dot{z}_n = \frac{H_1 \hat{s} f_S}{\sin\theta_S} i n Z_n + \hat{s}^2 \mu \dot{Z}_n, \quad at \quad \theta = \theta_S, \tag{14b}$$

where $\hat{s} = \left(H_1/H_2\right) < 1$ and $f_S = 2\Omega \cos\theta_S$.

The governing equations for Z_n and z_n are obtained by substituting equation (12) into equation (5):

$$A\ddot{Z}_n + B\dot{Z}_n - \left(n^2 + inC_2\right) Z_n = 0, \tag{15a}$$

$$A\ddot{z}_n + B\dot{Z}_n - \left(n^2 + inC_1\right) z_n = 0, \tag{15b}$$

where the superscript dot denotes a derivative with respect to θ. At the pole equation (8) requires that

$$Z_n = 0 \quad at \quad \theta = 0, \tag{16}$$

and on the boundary of the basin

$$z_n = \hat{z}_n = \hat{a}_n + i\hat{b}_n \quad at \quad \theta = \theta_B, \tag{17}$$

where

$$\left. \begin{array}{l} \hat{a}_n = \frac{1}{\pi} \int_0^{2\pi} \varphi_B \cos(n\varphi)\, d\varphi, \\ \hat{b}_n = \frac{1}{\pi} \int_0^{2\pi} \varphi_B \sin(n\varphi)\, d\varphi, \end{array} \right\} \quad n \geq 1 \tag{18a}$$

and

$$\hat{a}_0 = \frac{1}{2\pi} \int_0^{2\pi} \varphi_B\, d\varphi. \tag{18b}$$

For a polar basin with zero net transport into the domain equations (7) and (18b) reveal that $\hat{a}_0 = 0$. Now a_0 and A_0 are associated with an axisymmetric swirling flow in the $\hat{\varphi}$ direction over the shelf and in the deep basin. Across the straits the imposed transport is meridional (i.e., in the $\hat{\theta}$ direction) and so, following Imawaki and Takano (1974), we demand a_0 and A_0 are identically zero.

The general solutions of equation (15) are

$$z_n = f_n e^{\lambda_1 \theta} + g_n e^{\lambda_2 \theta}, \tag{19a}$$

$$Z_n = F_n e^{\omega_1 \theta} + G_n e^{\omega_2 \theta}, \tag{19b}$$

where λ_1, λ_2 are given by

$$\left. \begin{array}{l} \lambda_1 \\ \lambda_2 \end{array} \right\} = \frac{-B}{2A} \pm \frac{1}{2A} \{B^2 + 4A(n^2 + inC_1)\}^{1/2}, \tag{20}$$

and ω_1, ω_2 are given by equation (20) with C_1 replaced by C_2. Coefficients f_n, F_n, g_n and G_n are constants to be determined by applying the boundary and matching conditions. Application of equations (14), (16), and (17) yields

$$F_n + G_n = 0, \tag{21a}$$

$$f_n e^{\lambda_1 \theta_B} + g_n e^{\lambda_2 \theta_B} = \hat{z}_n, \tag{21b}$$

$$f_n e^{\lambda_1 \theta_S} + g_n e^{\lambda_2 \theta_S} = F_n e^{\omega_1 \theta_S} + G_n e^{\omega_2 \theta_S}, \tag{21c}$$

$$\begin{array}{l} f_n e^{\lambda_1 \theta_S} \left(\dfrac{in H_1 f_S}{\sin \theta_S} + \mu \lambda_1 \right) + g_n e^{\lambda_2 \theta_S} \left(\dfrac{in H_1 f_S}{\sin \theta_S} + \mu \lambda_2 \right) = \\ F_n e^{\omega_1 \theta_S} \left(\dfrac{in \hat{s} H_1 f_S}{\sin \theta_S} + \mu \hat{s}^2 \omega_1 \right) + G_n e^{\omega_2 \theta_S} \left(\dfrac{in \hat{s} H_1 f_S}{\sin \theta_S} + \mu \hat{s}^2 \omega_2 \right). \end{array} \tag{21d}$$

It is straightforward to solve equation (21) for the coefficients f_n, g_n, F_n, and G_n and subsequently the coefficients a_n, A_n, b_n, and B_n in equation (12) using equation (19).

Figures 2a and 2b show contours of the streamfunction (12) in a polar basin with a step shelf for which $H_1 = 250$ m, $H_2 = 1,000$ m, $\theta_S = 10°$, and the strength of the source/sink is 5 Sv representing the inflow from the Nordic strait (Beszczynska-Müller et al., 2012). The "large" bottom friction case, $\mu = 10^{-2}$ ms^{-1}, corresponds to the time scale of the decay of the solution $T \sim H\left(\mu^{-1}\right) \sim 10^5$ s to 1 day, while "small" bottom friction case with $\mu = 10^{-4}$ ms^{-1} corresponds to the decay time scale $\sim$100 days. When the bottom friction is small the ocean basin is effectively an annulus of uniform depth. The shelf break acts as a rigid boundary. Imagine turning on the source/sink and spinning-up the ocean to a steady state. The only subinertial waves supported in this domain are the planetary waves which spin-up the ocean circulation as shown in Figure 2b. Therefore, the structure of the circulation on the shelf is identical to that calculated by Imawaki and Takano (1974) in a flat bottom polar basin. However, with much larger bottom friction (see Figure 2a) the interior deep ocean basin is not dynamically isolated from the shelf and the basin now supports both planetary waves and subinertial topographic Rossby wave (TRW) modes that decay in amplitude with increasing meridional distance from the basin boundary and increasing meridional distance measured from either side of the shelf break. Consider once again switching on the source-sink pair in an ocean basin at rest when bottom friction is "large." The TRW modes (there are an infinite countable number of TRW modes supported by a step shelf
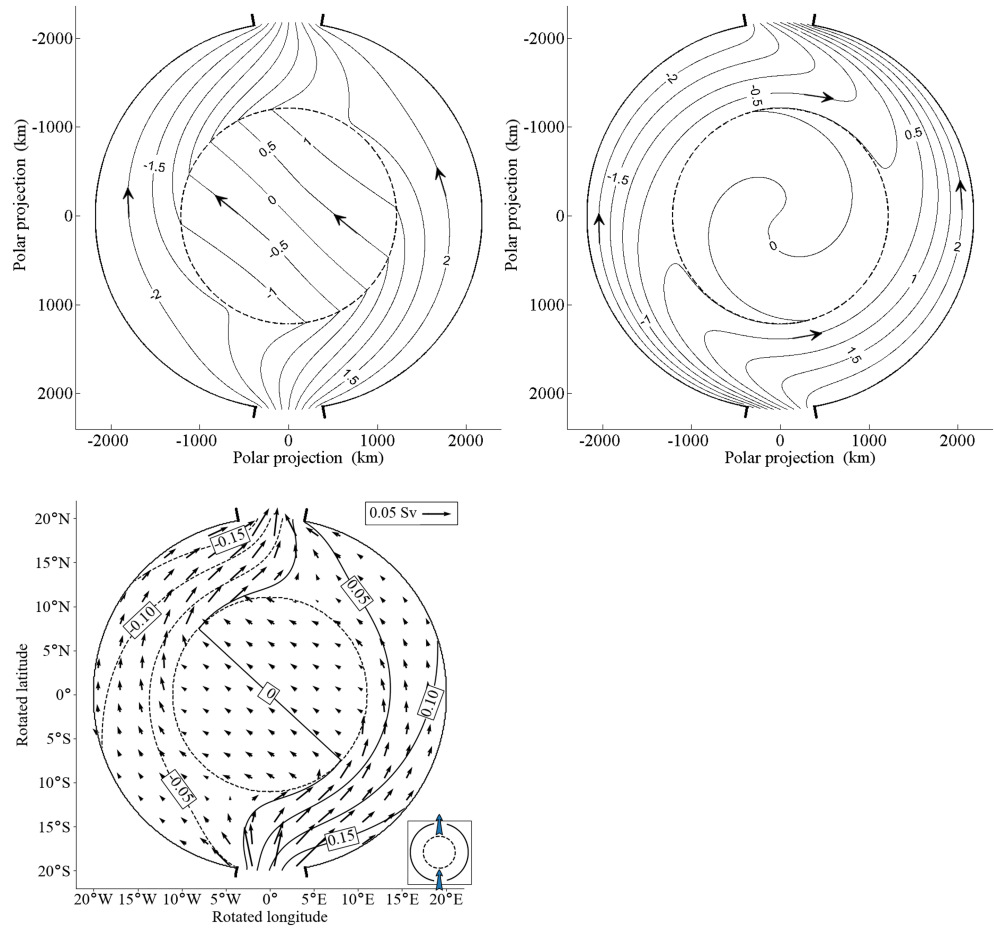
Figure 2. Plot of the streamfunction (12) corresponding to source-sink-driven planetary geostrophic flow in a polar basin with a step shelf and linear bottom friction when (a) $\mu = 10^{-2}$ m s^{-1}; (b) $\mu = 10^{-4}$ m s^{-1}. Plot (c) is the equivalent NEMO simulation to (a) where vectors represent the transport and the contours are sea surface elevation. Note that the shelf edge θ_S is contoured with dashed line.

characterized by the azimuthal wave number; Willmott and Bassom, private communication, April 2020) now contribute to the final spun-up state as seen by the deflection of the circulation in a clockwise direction at both straits (i.e., the azimuthal phase velocity of TRWs is counterclockwise). Transpolar irrotational circulation (i.e., zero relative vorticity) is present in the deep basin supported by a frictional boundary layer centered on the shelf break that supports a meridional transport of fluid between the shelf and the deep basin. Figure 2c shows the equivalent numerical solution using the NEMO model to that shown in Figure 2a revealing that the approximate analytical solution is in good agreement with the numerical solution.

Further insight about the dynamics of the steady-state circulation shown in Figure 2 can be obtained by integrating the curl of the momentum equations (1) over the deep basin:

$$\iint_S \nabla \times (f \mathbf{k} \times \mathbf{u}) \cdot d\mathbf{S} = -\frac{\mu}{H_2} \iint_S (\nabla \times \mathbf{u}) \cdot d\mathbf{S}, \tag{22}$$

where S is the surface area of the deep basin and $d\mathbf{S} = \mathbf{k} dS$. Linear bottom friction is employed in (22) and the wind stress is neglected. Application of Stokes's Theorem to the left-hand side of equation (22) reveals that

$$f_s \oint_C v \, dl = -\frac{\mu}{H_2} \iint_S \xi \, dS, \tag{23}$$

where $\xi = \mathbf{k} \cdot \nabla \times \mathbf{u}$ is the relative vorticity, and v is the meridional velocity component (i.e., normal to the shelf break) and C is the shelf break (i.e., $\theta = \theta_S$). Clearly, in steady state

$$\oint_C v \, dl = 0,$$

in which case the circulation in the deep basin must satisfy the integral constraint

$$\iint_S \xi \, dS = 0, \tag{24}$$

which leads to three possibilities. First, the interior circulation is stagnant in which case $\xi \equiv 0$ at all points in S. Second, the circulation is nonzero and irrotational inside the deep basin. Third, the circulation in S has regions in which ξ is positive and regions in which it is negative and which satisfy the integral constraint (24). Figure 2a, and the equivalent NEMO simulation of Figure 2c, is an example in which the (weak) deep basin circulation is irrotational.

In reality the width of the continental shelf in the Arctic basin is far from uniform. The Eurasian-Russian shelf is wider than the North American shelf on the western side of the Arctic basin. This motivates the following question: How will the source-sink circulation shown in Figure 2 be modified by a continental shelf of nonuniform width? The NEMO model is used to address this question. Indeed, this question is also motivated by the study of de Boer et al. (2018) who also consider the pathways of a transient pulse of water into the Arctic basin through the Bering Strait. The pulse of water is preferentially evacuated through the Nordic strait rather than the Canadian archipelago, which naturally leads to the question, "why?". Numerical process studies using NEMO suggest that the shelf geometry plays a crucial role in the transient adjustment of the Arctic basin to change in the transports through the Bering Strait (de Boer et al., 2018). This idea merits further attention here.

We consider three shelf configurations in the following numerical experiments. First, we consider a basin with a wide shelf (i.e., $\theta_S = 15°$) on the "eastern side" of the domain (i.e., $0 \leq \varphi \leq \pi$) and a narrow shelf (i.e., $\theta_S = 19°$) in the other half of the domain. There is a smooth transition between the narrow and wide shelves which spans the extent of the straits where a uniform source/sink are prescribed. Figure 3a shows contours of the surface elevation and the transport vectors associated with the steady-state source-sink-driven circulation in this basin. The grid resolution and bottom friction used in this numerical calculation are listed in Table 1. The basin used in Figure 3b is the reflection of that in Figure 3a about the diameter, $\varphi = 0$ and $\varphi = \pi$, resulting in a wide shelf on the "western side" ($\pi \leq \varphi \leq 2\pi$) of the domain. In both cases the majority of the source fluid is transported along the wide shelf (4.3 Sv of the incoming 5 Sv).

To understand this behavior in the weak bottom friction regime we observe that the deep basin is dynamically isolated from the shelf and the ocean domain is effectively a nonuniform width annulus. Where the annulus width is narrow, spanning only 1° of colatitude, the frictional boundary layers adjacent to the basin boundary and the shelf break, span the entire shelf. In a scenario where the source-sink are switched on and maintained, the planetary wave spin-up is essentially confined to the wide shelf, spanning 5° of colatitude; the waves are strongly damped on the narrow shelf. Therefore, the wide shelf supports the majority of the transport in Figures 3a and 3b.

Increasing the magnitude of bottom friction in the ocean basin shown in Figure 3a leads to the steady circulation plotted in Figure 3c. The deep ocean basin is no longer dynamically isolated from the shelf. On the narrow shelf the near-absence of any circulation results from high dissipation across this entire subdomain. On the wide "eastern" shelf TRWs are responsible for the subinertial spin-up of the circulation. Two distinctive features about the structure of the steady circulation are (a) fluid on the shelf crosses the shelf break via a frictional boundary layer to subsequently exit the basin at the sink-strait; (b) the majority of the fluid on the eastern shelf "drains" into the deep basin, with almost no fluid on the eastern shelf exiting the sink strait.

To emphasize the role of vorticity waves on these source-sink-driven flows, Figure 3d shows the steady circulation in a polar basin with a wide step shelf of limited azimuthal extent (i.e., spanning 90° of longitude) in the "eastern half" of the domain with small bottom friction used in Figures 3a and 3b. Following our earlier discussion, dynamically, the basin is effectively confined to a nonuniform width annulus. Now consider the scenario where the source-sink-driven flow is spun-up from rest. The extensive narrow shelf is a highly damped wave guide for planetary waves. On the confined wide shelf planetary waves are responsible for the spin-up. Thus, the circulation in Figures 3a and 3d is qualitatively similar. The narrow shelf regions on the "eastern half" of the basin connecting the wide shelf to the source and sink straits operate as damped wave
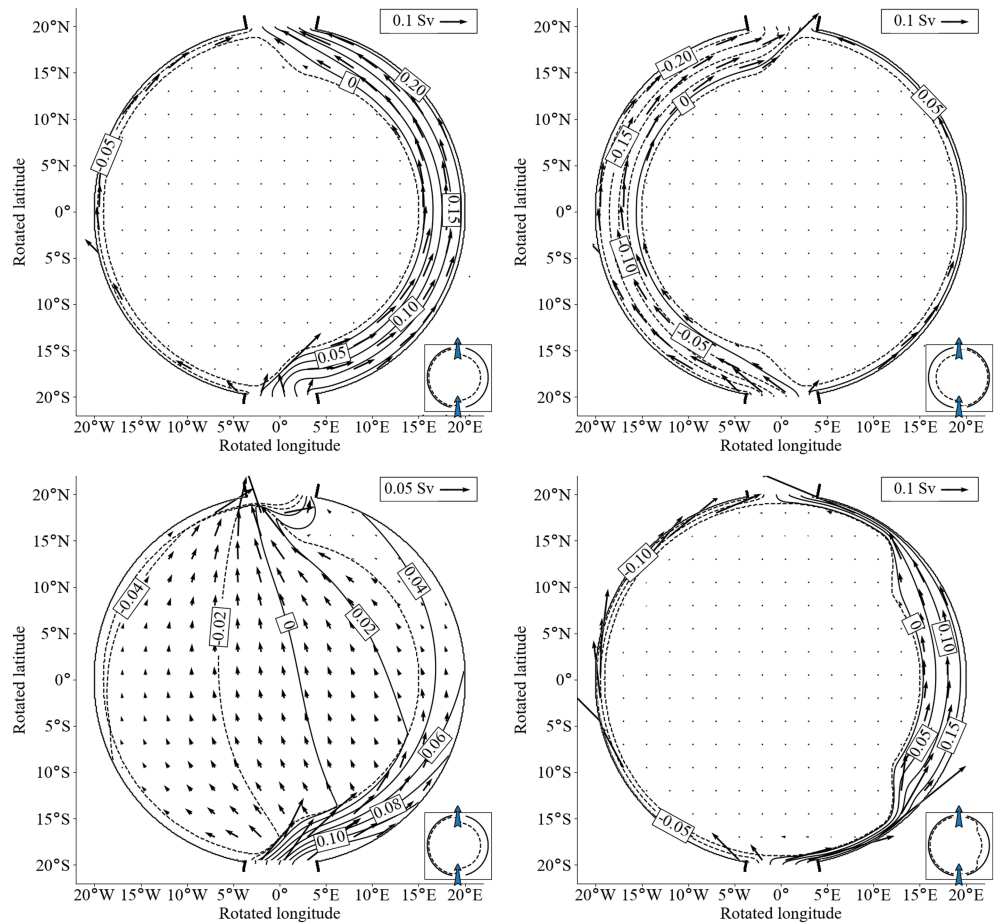
Figure 3. NEMO model simulation of steady source-sink-driven circulation in a polar basin with a nonuniform width shelf showing contours of the SSH and barotropic transport vectors. The box on the lower right-hand side of each panel shows the shelf geometry and the location of the source and sink. Plot (a) wide shelf occupying the entire "eastern" half of the basin with $\mu = 10^{-4}$ m s^{-1}; (b) as in (a) but for wide shelf on the "western" half of the basin; (c) as in (a) but for $\mu = 10^{-2}$ m s^{-1}; (d) wide shelf of more limited extent on the "eastern" half of the basin and $\mu = 10^{-4}$ m s^{-1}.

guides, effectively restricting the magnitude of the azimuthal cyclonic wide shelf transport to 3.3 Sv. The narrow western shelf connecting the source and sink straits supports a 1.7 Sv anticyclonic current.

3.3. Source-Sink-Driven Solutions in a Basin With a Step-Shelf in the Presence of Lateral Diffusion

In this section, we consider source-sink-driven flow in the presence of Laplacian friction in a circular polar basin with a step shelf. Qualitatively, the form of the circulation can be determined using the approximate form (2b) of the Laplacian diffusion operator. The diffusion terms retained in (2b) reflect the fact that the structure of the diffusive boundary layer adjacent to $\theta = \theta_B$ is controlled by the largest derivatives in the $\hat{\theta}$ direction. Use of equation (2b) greatly simplifies the analysis of the step shelf problem, in comparison with retaining the full diffusion operator, which was the approach taken by Imawaki and Takano (1974) for a flat bottom basin. Taking the curl of equation (1) we obtain the vorticity equation

$$\psi_{j\theta\theta\theta\theta} + P_1\psi_{j\theta\theta\theta} + P_2\psi_{j\varphi\varphi} - P_3\psi_{j\varphi\varphi\theta} + P_4\psi_{j\varphi\varphi\theta\theta} - P_5\psi_{j\varphi} = 0, \tag{25}$$

where

$$P_1 \equiv \cot\theta, \quad P_2 \equiv \frac{1 + \cos^2\theta}{\sin^4\theta}, \quad P_3 \equiv \frac{2\cos\theta}{\sin^3\theta}, \quad P_4 \equiv \csc^2\theta, \quad P_5 \equiv 2\Omega R^2 A_H^{-1}.$$

In equation (25), $\psi_j(j = 1, 2)$ denote the streamfunction on the shelf and in the deep basin, respectively. We note that $P_k(k = 1, .., 5)$ are depth independent. On the boundary of the basin we require that equation (7)

is satisfied, and in addition we impose the "no-slip" boundary condition

$$\psi_\theta = 0, \quad \text{at} \quad \theta = \theta_B. \tag{26}$$

At the pole we impose

$$\left.\begin{array}{c} \psi_{\varphi\varphi} = 0 \\ \psi_\theta = 0 \end{array}\right\} \quad \text{at} \quad \theta = 0. \tag{27}$$

The first of equation (27) follows immediately from the evaluation of equation (25) at the pole, while the second of (27) ensures that the zonal velocity vanishes (following Imawaki & Takano, 1974).

To complete the specification of the problem we impose four matching conditions at the shelf edge

$$\left.\begin{array}{c} \left[\psi_\theta\right] = \left[\psi_\varphi\right] = 0 \\ \left[fu + \dfrac{A_H}{R^2} v_{\theta\theta}\right] = 0 \\ \left[-fv + \dfrac{A_H}{R^2} u_{\theta\theta}\right] = 0 \end{array}\right\} \quad \text{on} \quad \theta = \theta_S. \qquad \begin{array}{l}(28a)\\[1.5em](28b)\\[1.5em](28c)\end{array}$$

Matching condition (28a) ensures that the transports tangential and normal to the shelf edge are continuous, and (28b) and (28c) ensure that the pressure, and its derivatives normal to the shelf edge, are continuous. In terms of ψ, equations (28b) and (28c) become

$$\left.\begin{array}{c} \left[\dfrac{f\psi_\theta}{H} + \dfrac{A_H}{R^2}\left(\dfrac{2\cos\theta}{\sin^2\theta}\psi_{\varphi\theta} - \dfrac{\psi_{\varphi\theta\theta}}{\sin\theta} - \dfrac{\left(1+\cos^2\theta\right)}{\sin^3\theta}\psi_\varphi\right)\right] = 0, \\[2em] \left[\dfrac{f\psi_\varphi}{H\sin\theta} - fv + \dfrac{A_H}{R^2}\psi_{\theta\theta\theta}\right] = 0, \end{array}\right\} \text{on } \theta = \theta_S, \qquad \begin{array}{l}(29a)\\[2em](29b)\end{array}$$

upon using (3). We seek solutions of (25) of the form (12) and follow the method of solution in section 3.2. For brevity, the derivation of the analytical solution is omitted and the reader is referred to Gavilan Pascual-Ahuir (2019) for further details.

Figures 4a and 4b show the contours for the streamfunction in a polar cap with a step shelf $H_1 = 250$ m, $H_2 = 1{,}000$ m, and $\theta_S = 10°$. In Figure 4a $A_H = 1{,}000$ m^2 s^{-1} and the circulation is confined to the shelf in a relatively narrow diffusive boundary layer. When A_H is increased to 10,000 m^2 s^{-1} the flow is still confined to the shelf, albeit in much wider boundary current. Note that the circulation in presence of bottom friction (Figure 2) is qualitatively similar with the boundary layer approximation as expected. The equivalent NEMO simulation to Figure 4a is shown in Figure 4c. Although the two solutions agree qualitatively, the NEMO solution is somewhat more diffused across the shelf. The analytical solutions retaining the full Laplacian diffusion operator, rather than the boundary layer approach adopted here, are indistinguishable from the solutions derived in this section and are therefore not presented, for brevity.

4. Wind-Driven Solutions
4.1. Flat Bottom Basin
We consider wind-driven circulation in the presence of bottom friction. The analysis proceeds as in section 3 except that the vorticity equations now take the form

$$\psi_{\varphi\varphi} + A\psi_{\theta\theta} + B\psi_\theta + C\psi_\varphi = \mu^{-1}R^2 H \sin^2\theta\{\mathbf{k}\cdot\nabla\times\boldsymbol{\tau}/\rho\}, \tag{30}$$

where the coefficients A, B, and C are defined in (6). Notice that in the absence of bottom friction (30) reduces to the Sverdrup balance

$$\frac{2\Omega}{R^2}\psi_\varphi = \mathbf{k}\cdot\nabla\times(\boldsymbol{\tau}/\rho), \tag{31}$$
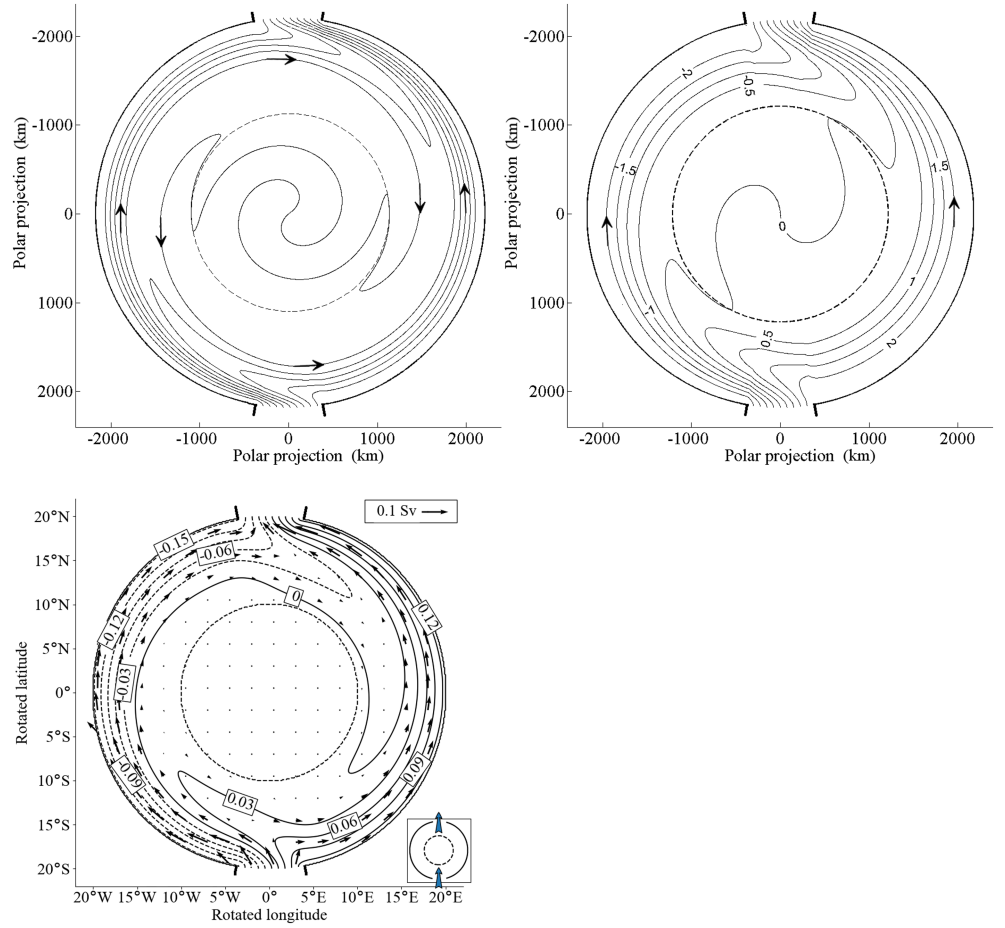
Figure 4. Plot of the streamfunction (23) corresponding to source-sink-driven planetary geostrophic flow in a polar basin with a step shelf and Laplacian eddy diffusivity when (a) $A_H = 1,000$ m^2 s^{-1}; (b) $A_H = 10,000$ m^2 s^{-1}. Plot (c) is the equivalent NEMO simulation to (b) where vectors represent the volume transport and the contours are sea surface elevation. Note that the shelf edge θ_S is contoured with dash marker.

which is instrumental in understanding the interior structure of the wind-driven circulation solutions derived below.

To make further progress in analytically solving (30) we consider a wind-stress curl distribution with two opposite signed cells:

$$\mathbf{k} \cdot \nabla \times (\boldsymbol{\tau}/\rho) = \frac{1}{\rho R \sin\theta} \left[(\sin\theta \tau^\varphi)_\theta - \tau^\theta_\varphi \right] \equiv \sin\left(\pi \frac{\theta}{\theta^*}\right) W(\varphi). \tag{32}$$

Clearly, this separable form of the wind stress curl vanishes at the pole and constant θ^* determines its meridional structure across the polar basin. We consider the following form for W:

$$W(\varphi) \equiv W_0 \begin{cases} -1 & \text{if} \quad 0 \le \varphi \le \hat{\varphi}_1 - \delta, \\ -1 + \left[\varphi - (\hat{\varphi}_1 - \delta) \right]/\delta & \text{if} \quad \hat{\varphi}_1 - \delta \le \varphi \le \hat{\varphi}_1 + \delta, \\ 1 & \text{if} \quad \hat{\varphi}_1 + \delta \le \varphi \le \hat{\varphi}_2 - \delta, \\ 1 - \left[\varphi - (\hat{\varphi}_2 - \delta) \right]/\delta & \text{if} \quad \hat{\varphi}_2 - \delta \le \varphi \le \hat{\varphi}_2 + \delta, \\ -1 & \text{if} \quad \hat{\varphi}_2 + \delta \le \varphi \le 2\pi, \end{cases} \tag{33}$$

where $W_0 = \tau_0/(\rho R)$ is the magnitude of the wind stress curl divided by density and τ_0 is a typical wind stress magnitude. Figure 5 shows a contour plot of (32), scaled by W_0, using the parameter values listed in Table 2 when $\hat{\varphi}_1 = \pi/2$ and $\hat{\varphi}_2 = 3\pi/2$.
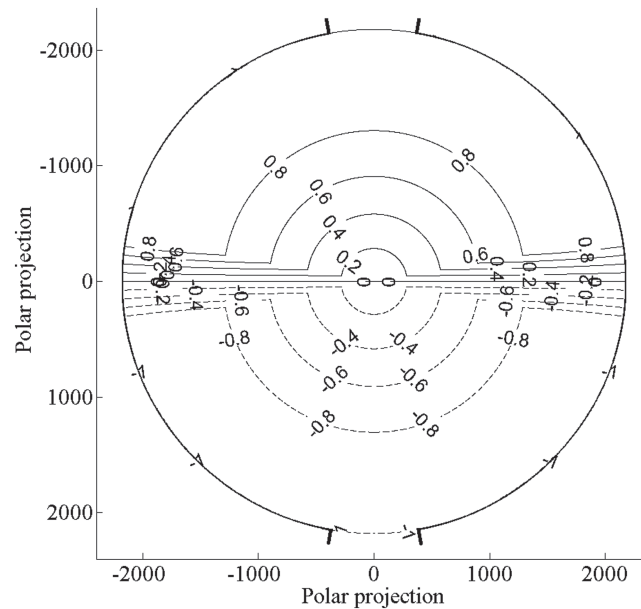
Figure 5. Contours of the wind stress curl (32) and (33) scaled by W_0. The continuous/dashed lines denote positive and negative values, respectively.

Before solving (30) we can deduce the qualitative behavior of the circulation with the aid of (31). The wind stress curl vanishes along the diameter defined by $\hat{\varphi}_1 = \pi/2$ and $\hat{\varphi}_2 = 3\pi/2$. On this diameter (31) requires that $v = 0$, at least away from the basin wall where a frictional boundary layer will be present. Thus, in the basin interior where the Sverdrup balance is valid, there will be two counterrotating circulation cells with axis of symmetry coinciding with the diameter $\varphi = \pi/2$ and $\varphi = 3\pi/2$. The circulation cells are closed by frictional wall boundary layers. As the magnitude of bottom friction increases the counterrotating cells rotate counterclockwise to eventually become aligned with the cells of the wind stress curl. This behavior was also noted by Willmott and Luneva (2015), albeit in a study using a polar beta plane.

Returning to the analysis of (30) we consider a polar basin with two diametrically opposite straits defined by $\theta = \theta_B$ and $-\epsilon \leq \varphi \leq \epsilon$ and $\pi - \epsilon \leq \varphi \leq \pi + \epsilon$. Across these straits we demand that the Sverdrup balance sets the meridional transport. Thus, at the open boundary $\theta = \theta_B, -\epsilon \leq \varphi \leq \epsilon$ the streamfunction takes the form

$$\psi = -\psi_0 \frac{\varphi}{\epsilon},$$

(34a)

where

$$\psi_0 = \frac{\epsilon R^2 W_0}{2\Omega} \sin\left(\pi \frac{\theta_B}{\theta^*}\right).$$

(34b)

Table 2
Parameter Values in the Idealixed Wind Stress Curl Function (32)

Symbol	Variable (unit)	Value
τ_0	Magnitude of the wind stress (N m^{-2})	0.1
R	Radius of the Earth (m)	6.370×10^6
ρ	Density (kg m^{-3})	1,025
δ	Angle subtended at the center at the domain of the wind stress curl transition zone (radians)	$\pi/18$
θ^*	Angle that controls the meridional structure of the curl(radians)	$4\pi/18$

Similarly, on the open boundary $\theta = \theta_B$, $\pi - \epsilon \leq \varphi \leq \pi + \epsilon$

$$\psi = \psi_0 \left[-1 + \frac{\varphi - (\pi - \epsilon)}{\epsilon} \right], \tag{35}$$

where ψ_0 is given by (34b). In summary, on the basin boundary the streamfunction must satisfy

$$\psi(\varphi, \theta_B) \equiv \psi_B(\varphi) = \psi_0 \begin{cases} -\varphi/\epsilon & \text{if} \quad |\varphi| \leq \epsilon, \\ -1 & \text{if} \quad \epsilon \leq \varphi \leq \pi - \epsilon, \\ -1 + [\varphi - (\pi - \epsilon)]/\epsilon & \text{if} \quad \pi - \epsilon \leq \varphi \leq \pi + \epsilon, \\ 1 & \text{if} \quad \pi + \epsilon \leq \varphi \leq 2\pi - \epsilon. \end{cases} \tag{36}$$

Once again, we seek a solution of (30) in terms of a Fourier expansion of the form (12) and therefore we decompose $W(\varphi)$ into a Fourier series:

$$W(\varphi) = p_0 + \sum_{n=1}^{\infty} \left[p_n \cos n\varphi + q_n \sin n\varphi \right]. \tag{37}$$

With $W(\varphi)$ prescribed by (33) we find that $q_n = 0$ $(n = 1, 2, ..)$ and

$$p_{2n-1} = \frac{4W_0}{\pi\delta} \frac{\sin\left[(2n-1)\delta\right]}{(2n-1)^2} (-1)^n \quad n = 1, 2, .. \tag{38}$$

and $p_0 = 0 = p_{2n}$ $(n = 1, 2, ..)$. Seeking a Fourier expansion solution for ψ and substituting (37) into (30) we obtain an inhomogeneous ordinary differential equation for Z_n defined in section 3.1:

$$A\ddot{Z}_n + B\dot{Z}_n - Z_n \left(n^2 + Cin \right) = \mu^{-1} R^2 H \sin^2\theta \sin\left(\pi \frac{\theta}{\theta^*} \right) W_n, \quad n = 1, 2, .. \tag{39}$$

where

$$W_n = p_n + iq_n. \tag{40}$$

The general solution of (39) takes the form

$$Z_n = R_n e^{\lambda_1 \theta} + S_n e^{\lambda_1 \theta} + Z_{nPI}, \tag{41}$$

where $\lambda_{1,2}$ are given by (20), R_n, S_n are arbitrary constants, and Z_{nPI} is a particular integral. Note that H_1 in (20) is replaced by H, the uniform depth of the basin. Determination of Z_{nPI} is routine but involves some lengthy algebra, and therefore the expression for this particular integral is given in Appendix A. To determine R_n, S_n we first decompose (36) into a Fourier series:

$$\psi_B = \sum_{n=1}^{\infty} \left[\hat{a}_n \cos n\varphi + \hat{b}_n \sin n\varphi \right], \tag{42}$$

noting that $\hat{a}_0 = 0$. Then

$$Z_n(\theta_B) \equiv \hat{Z}_n = \hat{a}_n + i\hat{b}_n, \tag{43}$$

and at the pole Z_n again satisfies (16). Application of (43) and (16) enables R_n and S_n to be determined. Finally, ψ is determined using (12) noting that the coefficients A_n, B_n are obtained from (41).

Figures 6a and 6b show contours of the analytical streamfunction when $\mu = 10^{-2}$ m s^{-1} and $\mu = 10^{-4}$ m s^{-1}, respectively. Figure 6c shows contours of the SSH calculated using NEMO, when $\mu = 10^{-4}$ m s^{-1} for comparison with Figure 6b. Model parameter values are listed in Tables 1 and 2. The circulation is characterized by two counterrotating gyres separated by a cross-basin current connecting the source to the sink. In the case of larger bottom friction the counterrotating gyres are displaced counterclockwise, the current is wider in the domain interior and the wall boundary layer circulation adjacent to the source/sink is wider. When
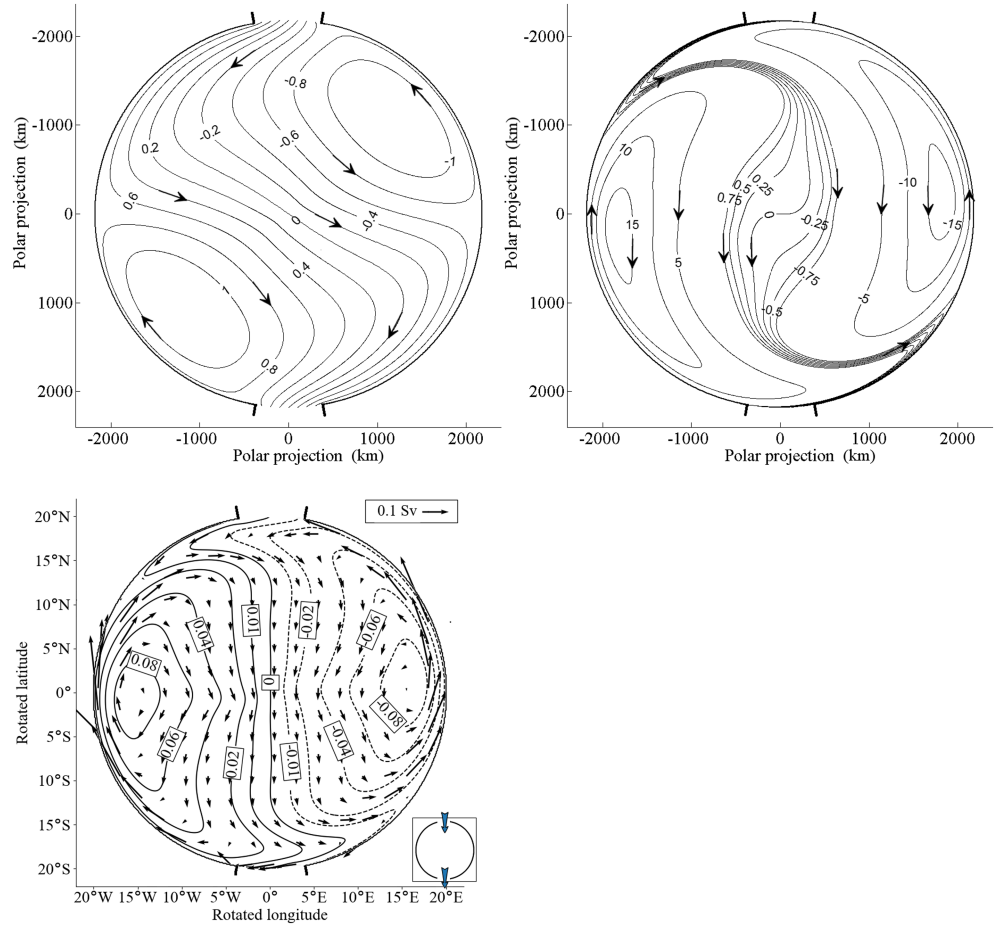
Figure 6. Plot of the streamfunction corresponding to wind stress-driven planetary geostrophic flow in a polar basin with linear bottom friction when (a) $\mu = 10^{-2}\ ms^{-1}$; (b) $\mu = 10^{-4}\ ms^{-1}$. Plot (c) is the equivalent NEMO simulation to (b) where vectors represent the volume transport and the contours are sea surface elevation.

μ is small the major axis of each gyre is approximately orthogonal to the diameter defined by $\varphi = \pi/2$ and $\varphi = 3\pi/2$. On this diameter, away from the narrow frictional wall boundary layers, the Sverdrup balance requires that $v = 0$ (recall v is the velocity component parallel to $\hat{\theta}$), which is clearly satisfied by the wind-driven gyres in Figure 6b. As μ increases the gyres rotate counterclockwise to become increasingly aligned with the wind-stress curl cells shown in Figure 5 because the Coriolis force becomes less important and nowhere in the domain is the circulation inviscid. There is a good qualitative agreement between the NEMO simulations of Figure 6c and the equivalent analytical solution in Figure 6b. Note that the NEMO simulation includes a small, but nonzero (i.e., $A_H = 500$ m^2 s^{-1}), Laplacian eddy diffusivity that leads to somewhat more diffusive gyres.

4.2. Step Shelf Solution

The solution of section 4.1 is now extended to include the step shelf first introduced in section 3. Adopting the notation of section 3.2, the wind-forced vorticity equations on the shelf (Region 1) and in the deep basin (Region 2) are

$$\psi_{j\varphi\varphi} + A\psi_{j\theta\theta} + B\psi_{j\theta} + C_j\psi_{j\varphi} = \mu^{-1}R^2H_j\sin^2\theta\{\mathbf{k}\cdot\nabla\times\boldsymbol{\tau}/\rho\}, \tag{44}$$

where $C_j = 2\Omega\mu^{-1}H_j\sin^2\theta$ and $j = 1, 2$.

We seek solutions of (44) of the form (12) for the two-cell wind stress curl (32) and (33). The reader is reminded that the coefficient a_n, b_n, A_n, and B_n are distinct to each subsection. Over the shelf and in the deep basin $z_n = a_n + ib_n$ and $Z_n = A_n + iB_n$, respectively, and they satisfy
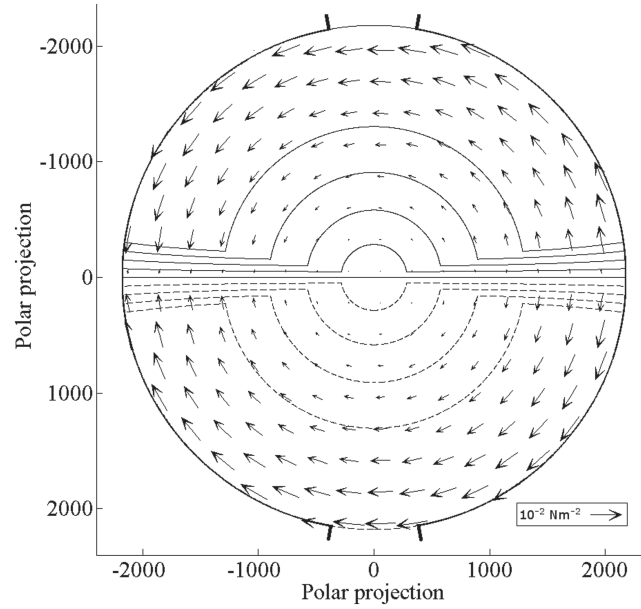
Figure 7. Plot of the azimuthal wind stress vectors given by (47).

$$A\ddot{z}_n + B\dot{z}_n - z_n\left(n^2 + inC_1\right) = \mu^{-1}R^2H_1\sin^2\theta\sin\left(\pi\frac{\theta}{\theta^*}\right)W_n, \tag{45a}$$

$$A\ddot{Z}_n + B\dot{Z}_n - Z_n\left(n^2 + inC_2\right) = \mu^{-1}R^2H_2\sin^2\theta\sin\left(\pi\frac{\theta}{\theta^*}\right)W_n, \tag{45b}$$

where the Fourier decomposition of the streamfunctions and the wind stress curl, discussed in section 4.1, have been utilized. On the boundary of the domain z_n satisfies (43), while at the pole Z_n must satisfy (17). To complete the streamfunction boundary value problem we must specify matching conditions at the shelf edge $\theta = \theta_S$. Continuity of the meridional transport across $\theta = \theta_S$ demands that $\left[\psi_\varphi\right] = 0$. Continuity of pressure at the shelf edge requires that

$$\left[fv + \mu\frac{u}{H} - \frac{\tau^\varphi}{\rho H}\right] = 0, \quad \text{at} \quad \theta = \theta_S. \tag{46}$$

Notice that the introduction of the step shelf gives rise to the presence of the azimuthal wind stress component $\tau^\varphi(\varphi, \theta)$ in (46). We hypothesize that the wind stress curl (32) is associated with a purely azimuthal wind stress, τ^φ, in which case

$$\frac{(\sin\theta\tau^\varphi)_\theta}{\rho R\sin\theta} = \sin\left(\frac{\pi\theta}{\theta^*}\right)W(\varphi).$$

Upon integrating with respect to θ we obtain

$$\tau^\varphi(\varphi, \theta) = \frac{\rho RW(\varphi)}{2\sin\theta}\left[\frac{\sin\left(\theta - \frac{\pi\theta}{\theta^*}\right)}{(1 - \pi/\theta^*)} - \frac{\sin\left(\theta + \frac{\pi\theta}{\theta^*}\right)}{(1 + \pi/\theta^*)}\right]. \tag{47}$$

Figure 7 shows a plot of the azimuthal wind stress field given by (47).

The shelf edge matching conditions can now be written in the form (13) and

$$\frac{H_1 f_S}{\sin\theta_S}inz_n + \mu\dot{z}_n - \frac{H_1 R^2 W_n\Theta\left(\theta_S\right)}{2\sin\theta_S} = \frac{H_1\hat{s}f_S}{\sin\theta_S}inZ_n + \hat{s}^2\mu\dot{Z}_n - \frac{\hat{s}H_1 R^2 W_n\Theta\left(\theta_S\right)}{2\sin\theta_S}, \quad \text{at} \quad \theta = \theta_S, \tag{48}$$

where W_n is given by (40) and

$$\Theta(\theta) \equiv \left[\frac{\sin\left(\theta - \frac{\pi\theta}{\theta^*}\right)}{(1 - \pi/\theta^*)} - \frac{\sin\left(\theta + \frac{\pi\theta}{\theta^*}\right)}{(1 + \pi/\theta^*)} \right]. \tag{49}$$

The general solutions of (45) take the form of

$$z_n = f_n e^{\lambda_1 \theta} + g_n e^{\lambda_2 \theta} + z_{nPI}, \tag{50a}$$

$$Z_n = F_n e^{\omega_1 \theta} + G_n e^{\omega_2 \theta} + Z_{nPI}, \tag{50b}$$

where λ_1, λ_2, ω_1, and ω_2 are defined in section 3.2 and the constants f_n, g_n, F_n, and G_n are to be determined by applying boundary conditions (16) and (43) and matching conditions (14) and (48). The particular integrals z_{nPI} and Z_{nPI} are given in Appendix A noting that over the shelf H and C are replaced by H_1 and C_1, respectively; in the deep basin H and C are replaced by H_2 and C_2, respectively.

Application of equations (16), (43), (14), and (48) yields

$$F_n + G_n + Z_{nPI}(0) = 0 \tag{51a}$$

$$f_n e^{\lambda_1 \theta_B} + g_n e^{\lambda_2 \theta_B} + z_{nPI}\left(\theta_B\right) = \hat{z}_n \tag{51b}$$

$$f_n e^{\lambda_1 \theta_S} + g_n e^{\lambda_2 \theta_S} + z_{nPI}\left(\theta_S\right) = F_n e^{\omega_1 \theta_S} + G_n e^{\omega_2 \theta_S} + Z_{nPI}\left(\theta_S\right), \tag{51c}$$

$$\begin{aligned}
&\left(\frac{H_1 f_S}{\sin\theta_S} in + \mu\lambda_1\right) f_n e^{\lambda_1 \theta_S} + \left(\frac{H_1 f_S}{\sin\theta_S} in + \mu\lambda_2\right) g_n e^{\lambda_2 \theta_S} + \frac{H_1 f_S}{\sin\theta_S} in z_{nPI}\left(\theta_S\right) + \mu \dot{z}_{nPI}\left(\theta_S\right) \\
&= \left(\frac{H_1 \hat{s} f_S}{\sin\theta_S} in + \mu\hat{s}^2 \omega_1\right) F_n e^{\omega_1 \theta_S} + \left(\frac{H_1 \hat{s} f_S}{\sin\theta_S} in + \mu\hat{s}^2 \omega_2\right) G_n e^{\omega_2 \theta_S} + \frac{H_1 \hat{s} f_S}{\sin\theta_S} in Z_{nPI}\left(\theta_S\right) \\
&+ \mu\hat{s}^2 \dot{Z}_{nPI}\left(\theta_S\right) + \frac{H_1 R^2 W_n \Theta\left(\theta_S\right)}{2\sin\theta_S}(1 - \hat{s}).
\end{aligned} \tag{51d}$$

Upon solving (51) for f_n, g_n, F_n, and G_n, the coefficients a_n, b_n, A_n, and B_n are determined from (50), and hence ψ_1, ψ_2 from (12).

Figures 8a–8c show contours of the analytic streamfunction when $\mu = 10^{-3}$, $\mu = 10^{-4}$ m s^{-1}, and $\mu = 10^{-5}$ m s^{-1}, respectively. Increasing bottom friction leads to the counterclockwise rotation of the wind-driven gyres on the shelf and in the deep basin. The equivalent NEMO numerical solution to Figure 8b is shown in Figure 8d and demonstrates that the approximate analytical solution captures the numerical solution well. Table 1 lists the NEMO model parameter values employed in Figure 8d.

Topographic steering has a profound impact on the path of the transpolar drift current (TDC) connecting the source strait to the sink strait. Fluid entering the source strait bifurcates on reaching the shelf edge to form "rim currents" that coalesce on the shelf diametrically opposite the divergence point. After the rim currents merge they exit the sink strait as an identifiable TDC. In more realistic numerical simulations of the Arctic Ocean circulation, Aksenov et al. (2016) also identify the presence of shelf break (i.e., rim) currents. In reality, it is likely that upper ocean stratification shields the TDC in the Arctic from topographic steering (Spall, 2016).

In the presence of wind stress (23) generalizes to

$$f_s \oint_C v dl = -\frac{\mu}{H_2} \iint_S \xi dS + \frac{1}{\rho H_2} \iint_S \nabla \times \boldsymbol{\tau} \cdot dS. \tag{52}$$

For the wind stress curl (32) the second term on the right-hand side of (52) vanishes because there are equal and opposite signed curl cells over the deep basin. Since the circulation in Figure 8 is steady the left-hand side of (52) vanishes, otherwise the deep-basin would fill or empty. Thus, (52) reduces to (24) must be satisfied by the dipole structure of the relative vorticity field in the deep basin.
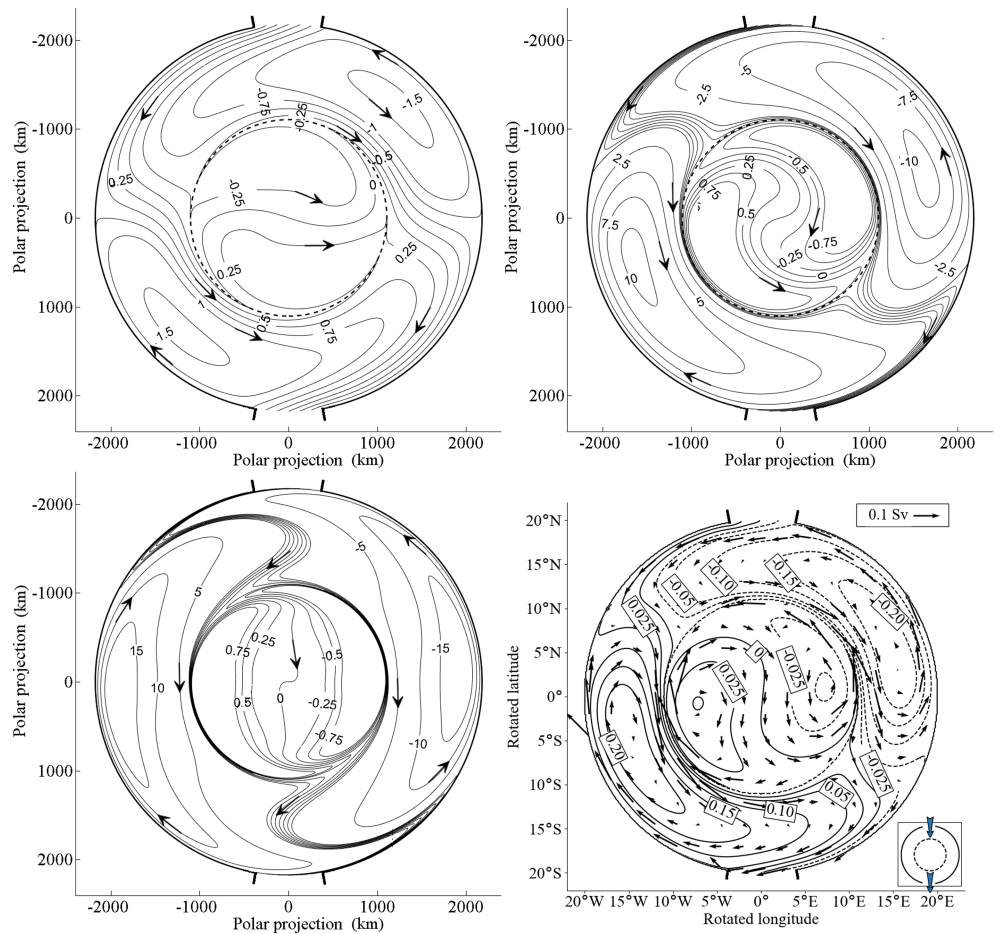
Figure 8. Plot of the streamfunction (22) corresponding to wind stress-driven planetary geostrophic flow in a polar basin with a step shelf and linear bottom friction when (a) $\mu = 10^{-3}$ m s^{-1}; (b) $\mu = 10^{-4}$ m s^{-1}; (c) $\mu = 10^{-5}$ m s^{-1}. Plot (d) is the equivalent NEMO simulation to (b) where vectors represent the volume transport and the contours are sea surface elevation. Note that the shelf edge θ_S is contoured with dash marker.

5. Numerical Simulations in a Basin with a Step Shelf, Transpolar Ridge and Straits

We now consider the wind-driven barotropic circulation in a prototype Arctic Ocean basin, building upon the examples in the previous sections. Figure 9 shows a schematic of the step-shelf basin with three straits representative of the Bering, Davis and Nordic Seas straits that is used in this section. The longitudinal extent of the three straits are defined by

$$\text{Nordic:} \quad \frac{-11\pi}{90} \leq \varphi \leq \frac{\pi}{10}$$

$$\text{Bering:} \quad \pi \leq \varphi \leq \frac{13\pi}{12}$$

$$\text{Davis:} \quad \frac{293\pi}{180} \leq \varphi \leq \frac{61\pi}{36}$$

The location of the three straits relative to the ridge (idealized Lomonosov Ridge) is representative of the Arctic Ocean basin geometry. In terms of kilometers the width of the Bering, Davis, and Nordic Seas are 620, 650, and 1,670 km, respectively. The shelf edge is defined by $\theta = 11°$ corresponding to a shelf width of approximately 900 km.

Proshutinsky and Johnson (1997) demonstrate that the atmospheric circulation over the Arctic frequently oscillates between two contrasting regimes characterized by the intensity of the anticyclonic high-pressure cell over the Beaufort Sea on a quasi-decadal time scale. A mathematical representation of these two wind
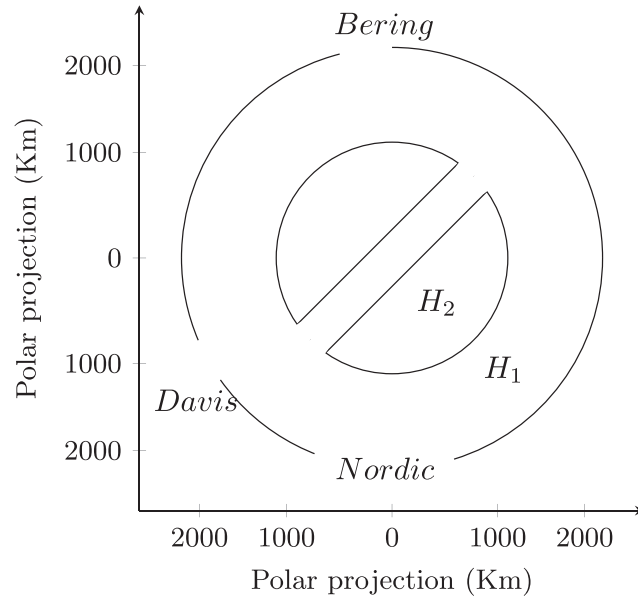
Figure 9. Schematic of a basin has three straits, a step shelf, and a ridge. The depths H_1 and H_2 are given in Table 1.

stress regimes is proposed, consisting of the linear superposition of two "building block" wind stress fields:

$$\tau^x = \alpha\tau^{x_1} + (1-\alpha)\,\tau^{x_2} \tag{53a}$$

$$\tau^y = \alpha\tau^{y_1} + (1-\alpha)\,\tau^{y_2} \tag{53b}$$

where the constant α satisfies $0 \leq \alpha \leq 1$.

The wind stress components τ^{x_1}, τ^{y_1} are referred to a Cartesian frame $O_1x_1y_1$ where O_1 is located at $[-500\ \text{km}, 900\ \text{km}]$ and O_1x_1 is parallel to Ox and O_1y_1 is parallel to Oy. The stress components are

$$\tau^{x_1} = \tau\frac{y_1}{r}\sin\left(\frac{r}{r_b}\pi\right), \tag{54a}$$
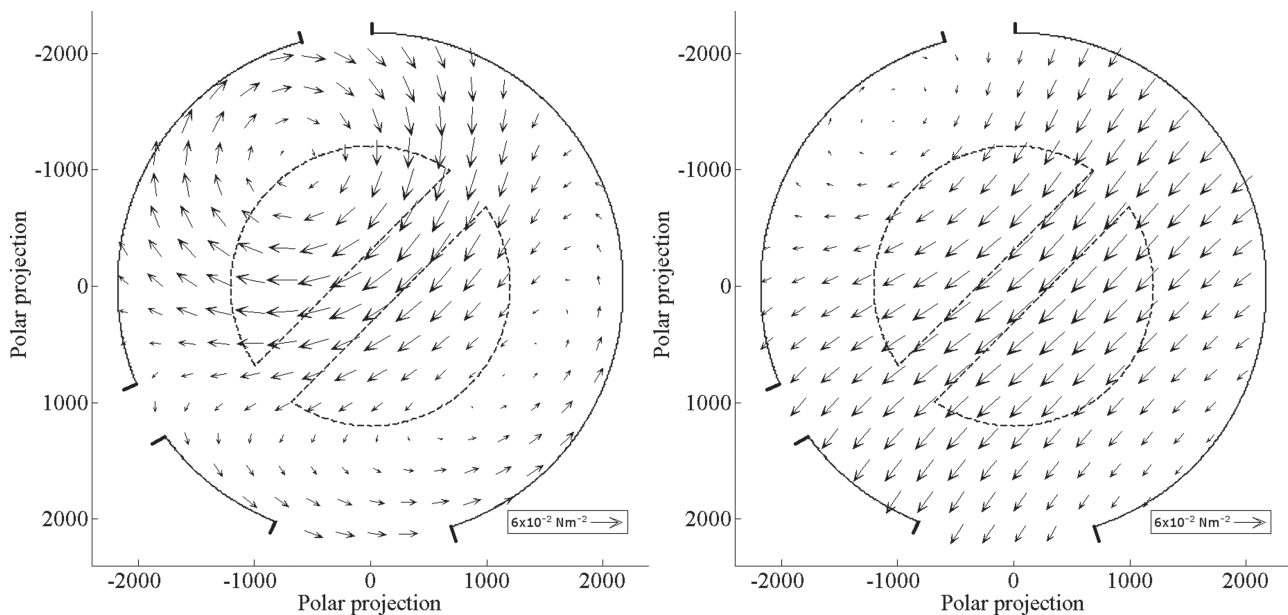

Figure 10. Plot of the wind stress vectors for (a) anticyclonic and (b) cyclonic regimes.
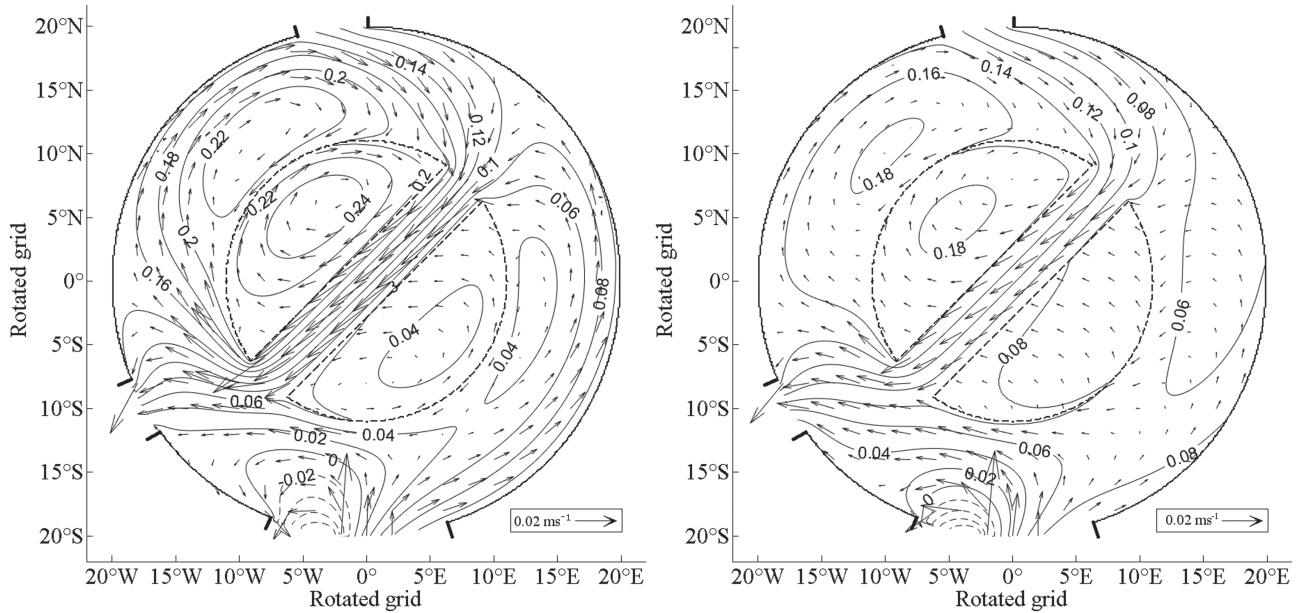
Figure 11. Contours of the sea surface elevation and barotropic ocean velocity vectors in a step-shelf basin with three straits and a top-hat transpolar ridge. Plot (a) is driven by an anticyclonic wind stress; (b) driven by cyclonic wind stress. Note that the shelf edge θ_S and the ridge are contoured with dash marker.

$$\tau^{y_1} = -\tau \frac{x_1}{r} \sin\left(\frac{r}{r_b}\pi\right), \tag{54b}$$

where r is distance from the origin O_1, r_b is the radius of the basin and $\tau = 0.07$ N m^{-2}. The wind stress (τ^{x_2}, τ^{y_2}) is a unidirectional wind stress field and is given by

$$\tau^{x_2} = -\frac{\tau}{\sqrt{2}} \sin\left(\left|\frac{y_2 \text{km} - 2,000 \text{ km}}{5,000 \text{ km}}\right|\pi\right), \tag{55a}$$

$$\tau^{y_2} = 0, \tag{55b}$$

In (55a) the Cartesian frame Ox_2y_2 is obtained by a 45° counterclockwise rotation of frame Oxy leading to the following coordinate relationships:

$$x_2 = \frac{1}{\sqrt{2}}(x+y) \tag{56a}$$

$$y_2 = \frac{1}{\sqrt{2}}(-x+y). \tag{56b}$$

The coefficient, α, for the anticyclonic and cyclonic wind stress regime was set to 0.7 and 0.2, respectively.

Figures 10a and 10b show plots of (53a) for an anticyclonic (e.g., 2007) and cyclonic (e.g., 1989) regime, respectively. There is also a seasonal signal in the structure of the Arctic wind stress field that favors an anticyclonic wind stress during the winter (Proshutinsky & Johnson, 1997).

The following numerical procedure is used to spin-up the circulation plotted in Figure 11. The Bering Strait inflow is prescribed and held constant throughout the numerical integration; its value is given in Table 3. Initially the volume transports across the Davis and Nordic straits are also prescribed as given in Table 3. As the numerical spin-up proceeds the values of Davis and Nordic straits transports are dynamically adjusted using the Flather (1994) open boundary condition which allows gravity waves to leave the domain correcting the boundary flows at each time step. Therefore, the spun-up transports across these two straits is different from their prescribed initial values. Table 3 presents the spun-up transport across these two straits.

Table 3
The Transport Boundary Conditions Initially Imposed Across the Straits in the NEMO Simulations Described in Section 5

Gap	Initial prescribed transport	Spun-up strait transport for the control simulation without wind stress	Spun-up strait transport for the anticyclonic wind regime	Spun-up strait transport for the cyclonic wind regime
Bering inflow	1	1	1	1
Davis outflow	−2.1	−3.393	−3.314	−3.623
Nordic inflow	6.5	4.839	4.868	5.068
Nordic outflow	−5.4	−2.446	−2.554	-2.445

Note. The Bering Strait transport is prescribed and held constant through the numerical integration. The transports across the Davis and Nordic Straits are allowed to adjust using a Flather open boundary condition. Note that the sign convection used to denote outflow from the basin is negative.

The circulation plotted in Figure 11a is driven by the anticyclonic wind stress. The key feature of the circulation in Figure 11a are as follows:

1. The transpolar ridge supports a topographically steered TDC in contrast to Figure 8, where the source and sink are connected by rim currents at the edge of the shelf.
2. Bering Strait inflow bifurcates into two branches; one feeds an intense anticyclonic gyre on the shelf while the second feeds the TDC. There is also a second deep-basin anticyclonic gyre in what would be termed "the western Arctic." In reality, the most conspicuous feature of the circulation in the western Arctic is the Beaufort Gyre (see Armitage et al., 2018). The fact that there is a single anticyclonic Beaufort Gyre points the importance of stratification shielding the upper ocean from topographic steering (Spall, 2016).
3. The Nordic Sea inflow bifurcates into three branches. One recirculates and exits through this strait and is qualitatively in agreement with the observed cyclonic GIN Sea gyre (Armitage et al., 2018). The second branch flows clockwise on the shelf and merges with the TDC to exit through the Davis Strait. In reality, the TDC exits the Arctic basin as the East Greenland Current. Furthermore, the real Canada shelf is much narrower than this idealized circular polar basin with a step-shelf Inclusion of more realistic basin topography would potentially address this deficiency in the process model. Finally, the third branch flows anticlockwise on the shelf merging with the TDC.
4. Topographic steering also leads to two cyclonic gyres in the eastern Arctic basin, whereas Armitage et al. (2018) show that a single cyclonic gyre is present in this region, indicating the importance of stratification.

The steady circulation driven by the cyclonic wind stress is plotted in Figure 11b. Qualitatively, all the features discussed in Figure 11a are still present with a notable reduction in the strength of the anticyclonic gyres on the shelf and in the deep basin. Kelly et al. (2018) plot the schematic surface circulation of the Arctic Ocean showing that water entering the Bering Strait bifurcates into three branches. Two of the branches feed the Transpolar Drift Current. The third branch, called the Alaskan Shelf-break Jet flows counterclockwise around the basin, north of the Canadian Archipelago. The modeled Arctic Ocean circulation in Figure 11 does not capture this latter current. Instead, water entering the basin through the Bering Strait is either entrained into the Beaufort Gyre or it follows a "central basin route" steered by the transpolar ridge to feed the Transpolar Drift Current. The Alaskan Shelf-break Current flows in the direction of coastally trapped topographic Rossby waves and its absence in Figure 11 reflects the dominance of the wind-driven circulation in this part of the domain.

6. Discussion

The approximate analytical approach for studying barotropic planetary geostrophic circulation in a circular polar basin, proposed by Imawaki and Takano (1974), is extended in this paper to include a step shelf and wind stress driving. The new analytical solutions presented in this paper are of interest to both the physical oceanographic and geophysical fluid dynamics communities. The analytical methods adopted in this study, and indeed the perturbation method discussed by Bassom and Willmott (2019), could be employed to develop solutions in a polar basin with somewhat more realistic topography.

Clearly, the neglect of stratification and sea ice limits the application of the solutions discussed in this paper. Turning to the latter point, the absence of summer sea ice may well occur by the middle of the 21st century (Jahn et al., 2016; Overland & Wang, 2013). Therefore, studies of wind, buoyancy, and boundary-forced

ocean circulation in a polar basin in the absence of sea ice takes on greater significance. In the Arctic, stratification shields the upper ocean from topographic steering (Boyd et al., 2002; Steele & Boyd, 1998). The topographical control is predominantly exerted on the part of the circulation that is not wind driven. Given the strong surface stratification, flows driven directly by the wind are confined to the upper ocean, the barotropic circulation being mostly a reflection of the thermohaline flows deeper down. In this paper the TDC relies on the existence of a transpolar ridge. When the top of the transpolar ridge is below the level of the shelf, an example not discussed in section 5 for brevity sake, the TDC is still present, albeit reduced in magnitude compared to that in Figure 11. Frictional boundary layers at the transpolar ridge shelf intersections support transport of fluid above the ridge in this case. The absence of stratification also leads to the two wind-driven anticylonic gyres "west" of the transpolar ridge in Figure 11, rather than the observed single Beaufort Gyre.

The impact of a variable width continental shelf on the pathways of the water connecting the source/sink straits deserves further analysis that is beyond the scope of this paper. Figure 3 suggests that the vorticity wave spin-up that establishes the steady-state circulation is extremely sensitive to the shelf width. This point was also noted in de Boer et al. (2018) and is not surprising. Wave scattering in the regions where the shelf width varies will lead to energy transfer between the vorticity wave modes (Wilkin & Chapman, 1987; Webster, 1987). Abrupt changes in the shelf width are more effective wave scatters (Webster, 1987). It appears that the refereed literature is restricted to barotropic shelf wave scattering by a single region in which the shelf width changes. However, in a circular basin of the type considered in this paper, two such scattering regions are present and this deserves further analysis.

Appendix A: The Particular Integral, Z_{nPI}, of Equation (41)

To obtain a particular integral of (41) the right-hand side of this equation is rewritten as

$$\frac{HR^2}{2\mu} W_n \left\{ \sin\left(\frac{\pi\theta}{\theta^*}\right) - \frac{1}{2}\sin\left(2\theta + \frac{\pi\theta}{\theta^*}\right) + \frac{1}{2}\sin\left(2\theta - \frac{\pi\theta}{\theta^*}\right) \right\} \tag{A1}$$

and it is now clear that Z_{nPI} will be a linear combination of three families of sin and cos functions with arguments appearing on the right-hand side of equation (A1). It is then straightforward to show that

$$\begin{aligned}
Z_{nPI} = \frac{HR^2}{\mu} W_n \Big\{ &E_{1n}\cos\left(\pi\frac{\theta}{\theta^*}\right) + E_{2n}\sin\left(\pi\frac{\theta}{\theta^*}\right) \\
&+ E_{3n}\cos\left[\left(2 + \frac{\pi}{\theta^*}\right)\theta\right] + E_{4n}\sin\left[\left(2 + \frac{\pi}{\theta^*}\right)\theta\right] \\
&+ E_{5n}\cos\left[\left(2 - \frac{\pi}{\theta^*}\right)\theta\right] + E_{6n}\sin\left[\left(2 - \frac{\pi}{\theta^*}\right)\theta\right] \Big\}
\end{aligned} \tag{A2}$$

where

$$E_{1n} = \left(-\frac{1}{2}\frac{\pi}{\theta^*}\right) B(DEN1)^{-1}$$

$$E_{2n} = -\frac{1}{2}\frac{TERM1}{DEN1}$$

$$E_{3n} = \frac{1}{4}(2 + \pi/\theta^*) B(DEN2)^{-1}$$

$$E_{4n} = \frac{TERM2}{4(DEN2)}$$

$$E_{5n} = -\frac{1}{4}(2 - \pi/\theta^*) B(DEN3)^{-1}$$

$$E_{6n} = -\frac{TERM3}{4(DEN3)}$$

and

$$TERM1 \equiv (\pi/\theta^*)^2 A + n^2 + inC$$

$$DEN1 \equiv (TERM1)^2 + (\pi/\theta^*)^2 B^2$$

$$TERM2 \equiv (2 + \pi/\theta^*)^2 A + n^2 + inC$$

$$DEN2 \equiv (TERM2)^2 + (2 + \pi/\theta^*)^2 B^2$$

$$TERM3 \equiv (2 - \pi/\theta^*)^2 A + n^2 + inC$$

$$DEN3 \equiv (TERM3)^2 + (2 - \pi/\theta^*)^2 B^2$$

References

Aksenov, Y., Karcher, M., Proshutinsky, A., Gerdes, R., de Cuevas, B., Golubeva, E., et al. (2016). Arctic pathways of Pacific water: Arctic Ocean model intercomparison experiments. *Journal of Geophysical Research: Oceans*, *121*, 27–59. https://doi.org/10.1002/2015JC011299

Armitage, T. W. K., Bacon, S., & Kwok, R. (2018). Arctic Sea level and surface circulation response to the Arctic Oscillation. *Geophysical Research Letters*, *45*, 6576–6584. https://doi.org/10.1029/2018GL078386

Bassom, A. P., & Willmott, A. J. (2019). Accurate approximations for planetary and gravity waves in a polar basin. *Tellus A*, *71*(1), 1–7. https://doi.org/10.1080/16000870.2019.1618133

Beszczynska-Müller, A., Fahrbach, E., Schauer, U., & Hansen, E. (2012). Variability in Atlantic water temperature and transport at the entrance to the Arctic Ocean, 1997–2010. *ICES Journal of Marine Science*, *69*(5), 852–863.

Boyd, T. J., Steele, M., Muench, R. D., & Gunn, J. T. (2002). Partial recovery of the Arctic Ocean halocline. *Geophysical Research Letters*, *29*(14), 2–1–2–4. https://doi.org/10.1029/2001GL014047

de Boer, A. M., Gavilan Pascual-Ahuir, E., Stevens, D. P., Chafik, L., Hutchinson, D. K., Zhang, Q., et al. (2018). Interconnectivity between volume transports through Arctic straits. *Journal of Geophysical Research: Oceans*, *123*, 8714–8729. https://doi.org/10.1029/2018JC014320

Flather, R. A. (1994). A storm surge prediction model for the northern Bay of Bengal with application to the cyclone disaster in April 1991. *Journal of Physical Oceanography*, *24*(1), 172–190.

Gavilan Pascual-Ahuir, E. (2019). Wind and boundary driven planetary geostrophic circulation in a polar basin (Ph.D. Thesis), University of Newcastle upon Tyne, Newcastle upon Tyne.

Imawaki, S., & Takano, K. (1974). Planetary flow in a circular basin. *Deep Sea Research and Oceanographic Abstracts*, *21*(1), 69–IN3.

Jahn, A., Kay, J. E., Holland, M. M., & Hall, D. M. (2016). How predictable is the timing of a summer ice-free Arctic? *Geophysical Research Letters*, *43*, 9113–9120. https://doi.org/10.1002/2016GL070067

Kelly, S., Popova, E., Aksenov, Y., Marsh, R., & Yool, A. (2018). Lagrangian modeling of Arctic Ocean circulation pathways: Impact of advection on spread of pollutants. *Journal of Geophysical Research: Oceans*, *123*, 2882–2902. https://doi.org/10.1002/2017JC013460

LeBlond, P. H. (1964). Planetary waves in a symmetrical polar basin. *Tellus*, *16*(4), 503–512.

Luneva, M. V., Willmott, A. J., & Maqueda, M. A. M. (2012). Geostrophic adjustment problems in a polar basin. *Atmosphere-Ocean*, *50*(2), 134–155. https://doi.org/10.1080/07055900.2012.659719

Madec, G. (2008). NEMO ocean engine. Note du Pole de modelisation de l'Institut Pierre-Simon Laplace (IPSL), 27.

Overland, J. E., & Wang, M. (2013). When will the summer Arctic be nearly sea ice free? *Geophysical Research Letters*, *40*, 2097–2101. https://doi.org/10.1002/grl.50316

Proshutinsky, A., & Johnson, M. (1997). Two circulation regimes of the wind-driven Arctic Ocean. *Journal of Geophysical Research*, *102*(C6), 12,493–12,514. https://doi.org/10.1029/97JC00738/abstract

Sakov, P., Counillon, F., Bertino, L., Lister, K. A., Oke, P. R., & Korablev, A. (2012). TOPAZ4: An ocean-sea ice data assimilation system for the North Atlantic and Arctic. *Ocean Science*, *8*(4), 633–656.

Spall, M. A. (2016). Wind-driven flow over topography. *Journal of Marine Research*, *74*(4-5), 229–248.

Steele, M., & Boyd, T. (1998). Retreat of the cold halocline layer in the Arctic Ocean. *Journal of Geophysical Research*, *103*(C5), 10,419–10,435. https://doi.org/10.1029/98JC00580

Webster, I. (1987). Scattering of coastally trapped waves by changes in continental shelf width. *Journal of Physical Oceanography*, *17*(7), 928–937.

Wilkin, J. L., & Chapman, D. C. (1987). Scattering of continental shelf waves at a discontinuity in shelf width. *Journal of Physical Oceanography*, *17*(6), 713–724.

Willmott, A. J., & Gavilan Pascual-Ahuir, E. (2017). Planetary and gravity waves in a polar basin. *Journal of Physical Oceanography*, *47*(6), 1433–1440. https://doi.org/10.1175/JPO-D-16-0253.1

Willmott, A. J., & Luneva, M. V. (2015). Steady, barotropic wind and boundary-driven circulation on a polar plane. *Geophysical & Astrophysical Fluid Dynamics*, *109*(3), 216–233. https://doi.org/10.1080/03091929.2015.1050589

Zhao, B., & Timmermans, M.-L. (2018). Topographic Rossby waves in the Arctic Ocean's Beaufort Gyre. *Journal of Geophysical Research: Oceans*, *123*, 6521–6530. https://doi.org/10.1029/2018JC014233